Acta Materialia 166 (2019) 148–157

Contents lists available at ScienceDirect

Acta Materialia

journal homepage: www.elsevier.com/locate/actamat

Full length article

Stability and strain-driven evolution of β′ precipitate in Mg-Y alloys

Ellen L.S. Solomon [a], Anirudh Raju Natarajan [b], Arunabha Mohan Roy [c], Veera Sundararaghavan [c], Anton Van der Ven [b], Emmanuelle A. Marquis [a, *]

[a] Department of Material Science and Engineering, University of Michigan, Ann Arbor, MI, 48109, USA
[b] Materials Department, University of California, Santa Barbara, CA, 93106, USA
[c] Department of Aerospace Engineering, University of Michigan, Ann Arbor, MI, 48109, USA

ARTICLE INFO

Article history:
Received 21 September 2018
Received in revised form
10 December 2018
Accepted 13 December 2018
Available online 14 December 2018

Keywords:
Mg alloy
Precipitation
Strain energy
Phase stability

ABSTRACT

Alloying Mg with rare-earth elements, such as Nd, Gd, or Y, enables hardening from the precipitation of metastable coherent phases during aging at low temperatures. While the aging potential of binary Mg-Nd alloys is relatively limited due to the nucleation of coarse β_1 and β precipitates at the expense of the strengthening β‴ precipitates, binary Mg-Y alloys exhibit exceptional stability of the strengthening coherent β_S' phase when aged at 200 °C. Through combination of high-resolution characterization, density functional theory calculations, and finite-element elasticity studies, we demonstrate that the strengthening β_S' phase is thermodynamically stable at low temperatures (as opposed to metastable as in other Mg-RE binaries) and that misfit strains play a key role in not only controlling precipitate structure and morphology but also their unusual evolution into an interconnected network.

1. Introduction

Magnesium rare-earth alloys can achieve exceptional strength when age-hardened at temperatures below 473 K, making them very attractive for structural applications where weight is an important factor [1–3]. Aging binary Mg-RE alloys (RE = Nd, Y, Gd, Sm, or Dy) below 473 K leads to the formation of GP zones, followed by one or more metastable ordered phases, including β′, β‴, and β_1, before the stable β phase appears. The β′ phase is found in binary Mg-Y [4] and Mg-Dy [5] alloys, while β‴ is found in binary alloys containing Nd [5,6], Gd [7,8], and Sm [9] – in both cases, these coherent precipitates, which are commonly believed to be metastable, are associated with peak hardness. The β′ and β‴ phases actually correspond to families of orderings over the sites of hcp [10,22]. The β′ orderings consist of zig-zag rows of rare earth atoms, with β_P' (β_S') referring to an ordering where successive zig-zag rows are aligned in phase (out of phase) with respect to each other [10]. The β‴ orderings are derived from the β′ orderings in that they have rare earth atoms arranged as strips of hexagons interleaved at different intervals between the zig-zag rows of β' [10,22]. The selection of β′ or β‴ is a function of the associated misfit strains [10] that also affect precipitate shapes [11,12] leading to different precipitate morphologies in each alloy system. In Mg-Nd alloys, the β_P' precipitates form as plates with habit planes lying parallel to $\{11\bar{2}0\}_{Mg}$ planes extending in the [0001] Mg direction [13]. In Mg-Gd, β_S' precipitates are globular $[0001]_{Mg}$ rods [8], while the β_S' precipitates form as rods with square cross sections in Mg-Y alloys [8].

Beyond equilibrium precipitate structure and shape, stability and evolution during aging are important factors to consider for long-term applications. The isothermal aging behavior is most often quantified using microhardness measurements and selected microstructural observations at relevant aging times. At 473 K, Mg-Nd alloys have limited peak hardness increase that is quickly achieved after about 1 h of aging [14]. This is due to premature nucleation of larger β_1 precipitates associated with dissolution of the β‴ precipitates and loss of strength [15]. On the other hand, Mg-Gd and Mg-Y alloys exhibit more significant hardening behavior with delayed peak hardness at about 1000 h for Mg-Gd alloys [16] to beyond 1000 h for Mg-Y alloys [15]. This behavior may be partly explained by the lack of β_1 observed in these alloys as well as the slow kinetics of precipitation. While precipitation evolution in binary Mg-Nd alloys during aging at 200 °C has been well characterized [5,6,17,18], and a few studies followed the evolution of β_S' precipitates in Mg-Gd alloys [7,8,19], the aging behavior of Mg-Y alloys is comparatively much less characterized.

According to existing literature, the precipitation sequence in

* Corresponding author.
E-mail address: emarq@umich.edu (E.A. Marquis).

https://doi.org/10.1016/j.actamat.2018.12.026
1359-6454/

Mg-Y is currently reported as follows [4,17,20,21]:

SSSS → solute clusters → GP zones (single monolayers) → β_S' → β

Nishijima first reported the structure of β′ precipitates using HAADF-STEM imaging of Mg-Y alloys aged at 473 K for 336 h, revealing isolated precipitates with Y atoms ordered over a subset of the sites of hcp that can adopt three distinct orientational variants [4]. GP zones consisting of single sheets of ordered Y atoms were reported to form at 323 K prior to β' precipitates [20]. The β phase, $Mg_{24}Y_5$, was observed after aging at 623 K [21]. The time scale required for β nucleation is unknown due to a limited number of aging studies in the lower temperature range (<473 K). From these isolated studies, the precipitation evolution and aging potential of Mg-Y alloys remains unclear.

This work seeks to develop a better understanding of phase stability in the Mg-Y binary and to establish the precipitate evolution during aging at 473 K. Through combination of high-resolution characterization, density functional theory calculations, and finite-element elasticity studies, we demonstrate that the strengthening β' phase is thermodynamically stable at low temperatures (as opposed to metastable as in other Mg-RE binaries) and that misfit strains play a key role in not only controlling precipitate structure and shape but also their coarsening behavior. Consequently, misfit strains provide an additional handle to tailor Mg-rare earth alloy microstructures and control their aging behavior.

2. Experimental

The alloy was provided by Magnesium Elektron North America Inc. The composition was measured to be Mg-7.47 wt.% Y (Mg-2.16 at.% Y) by inductively coupled plasma mass spectrometry. Samples were sectioned, encapsulated in quartz tubes in an argon atmosphere, and solution treated at 834 K for 24 h followed by water quenching. Samples were then aged in an oil bath at 473 K for times ranging between 0 and 13,000 h followed by water quenching.

Samples for Vicker's microhardness measurements were mounted in epoxy and ground flat with SiC paper in the following order: 400, 600, 800, and 1200 grit. Mirror finish surfaces were achieved after final polishing with 3 μm and 1 μm diamond suspensions and 0.05 μm colloidal silica. Vickers microhardness measurements were carried out at a load of 100 g and dwell time of 15 s.

Samples for TEM analysis were prepared either by twin-jet electropolishing using the method described in Ref. [22] or using focused-ion beam (FIB) milling. Micrographs were taken using a JEOL 2100 operated at 200 kV with a collection angle of 52 mrad or a double-corrected JEOL 3100R05 microscope operated at 300 kV with a collection angle of 74 mrad. The β' precipitates were measured from STEM images using ImageJ [76].

3. Computational methods

3.1. First-principles calculations

Equilibrium phases at elevated temperatures were determined by minimizing the free energy over all relevant phases. Here, we explored the role of occupation degrees of freedom at 0 K and vibrational degrees of freedom on the phase stability in the Mg-Y system. First-principles electronic structure calculations were carried out with the Perdew-Burke-Ernzerhof (PBE) parameterization of the generalized gradient approximation (GGA) to density functional theory (DFT). Projector augmented wave (PAW) pseudopotentials were used to calculate total energies for structures with the Vienna Ab-Initio Simulation. An energy cutoff of 450 eV was used with a Γ-centered 25 × 25 × 13 k-point mesh for the hcp unit cell. Calculations of supercell orderings on hcp were performed with k-point meshes that had an equivalent density per k-point in reciprocal space. Total energies of compounds were calculated by relaxing internal degrees of freedom, cell shape and volume. Pseudopotentials containing eight valence electrons for Mg and eleven electrons for Y were used.

To understand the role of ordering in the Mg-Y binary alloy, we calculated the formation energies of symmetrically distinct orderings on a number of different crystal structures. Formation energies were calculated relative to the zero Kelvin total energies of HCP Mg and Y as:

$$E(\vec{\sigma}) = \frac{E^{DFT}(\vec{\sigma}) - N_{Mg}E_{Mg} - N_Y E_Y}{N_{Mg} + N_Y}$$

Metastable equilibrium at zero Kelvin was estimated by using the convex hull construction on the set of configurations that did not undergo large distortions. Global equilibrium was determined by using all the structures in the calculations. Experimentally, the binary alloy is reported to form phases on the HCP, C14-Laves phase, BCC and α-Mn crystal structure prototypes [23]. Symmetrically distinct orderings were constructed on all four parent crystal structures using the CASM software package [24,25, 26].

Vibrational contributions to the free energies were calculated at elevated temperatures within the quasiharmonic approximation. Symmetrically distinct perturbations were applied to atoms within each crystal and forces were estimated with VASP in large cells containing at least 96 atoms. Perturbations were applied in cells with volumes that ranged from −2 to 6% relative to the equilibrium volume under zero external pressure. Hexagonal cells were manually optimized to obtain the equilibrium $\frac{c}{a}$ ratios. K-point meshes were scaled appropriately for the larger cells to maintain the same linear mesh density. Force constants obtained from a least-squares fit to the calculated forces were used to construct the dynamical matrix for each structure and volume in order to calculate vibrational frequencies and phonon densities of states, which were then used to calculate the Helmholtz free energy as a function of volume. The Gibbs free energy at zero pressure was estimated as the minimum of the Helmholtz free energies as a function of volume at different temperatures.

3.2. Finite element method

To confirm the hypothesis that the precipitation evolution behavior described in Section 4.2 corresponds to a strain energy dominated aging process, Finite Element Method (FEM) analysis was performed to determine the elastic response of the microstructure. We considered deformation in a microstructure of finite size, which was fixed at the external surfaces (corresponding to embedded grain in a polycrystal) and was loaded via the misfit strain (ε_0) of the precipitates [27–29]. The simulations were carried out under plane strain conditions by discretizing the microstructure measured on the basal plane using 10,000 four noded quadrilateral elements. The equivalent mechanical force of each element, {F}, is given by:

$$\{F\} = \int [B]^T [D]\{\varepsilon_0\} dV$$

where [B] is the strain-displacement matrix, [D] is the material stiffness matrix, $\{\varepsilon_0\}$ is the initial strain (as a vector in Voigt notation). We considered three different variants of the precipitate at 0, 60 and 120 degrees on the basal plane. The stiffness and

transformation strains of the precipitates were rotated so as to match the sample coordinate system of x-axis parallel to $[11\bar{2}0]$ and y -axis parallel to $[\bar{1}100]$. Note that the matrix properties need not be transformed about the basal plane due to transverse isotropy. The strain energy density of each element was then computed using the calculated stress ($\{\sigma\}$ as a Voigt vector) as $E = \{\varepsilon - \varepsilon_0\}^T\{\sigma\}$. The misfit strains ($\varepsilon_0$) for different variants and full 6×6 anisotropic stiffness matrix for both the matrix (hexagonal symmetry) and precipitates (orthorhombic symmetry) were obtained from previous DFT simulations [10].

4. Results

We first summarize the results of a first principles study of phase stability in the Mg-Y binary, which, contrary to common assumptions, indicates that the strengthening phase, β_S', of dilute Mg-Y alloys is a thermodynamically stable phase at intermediate to low temperatures. Next we describe aging experiments that reveal the microstructural evolution of coherent β_S' precipitates in dilute Mg-Y alloys as a function of time, and end with a finite element analysis of the strain energy of different configurations of coherent precipitates.

4.1. Predicted Mg-Y phase diagram

We started by establishing phase stability at zero Kelvin. Fig. 1a shows the formation energies calculated with density-functional theory for symmetrically distinct orderings on the HCP, BCC, C14-Laves and the α-Mn crystal structures. The convex hull connecting the stable phases at zero Kelvin is shown as dashed lines in Fig. 1a. The ground states at zero Kelvin consist of β′-Mg_7Y, which is an ordering on HCP, and the two BCC based orderings β_1 ($L2_1$) Mg_3Y and B2 MgY. Interestingly, the experimentally observed Laves phase and the $Mg_{24}Y_5$ phase are not predicted to be stable at 0 K. Furthermore, the predicted ground states at 0 K are not observed experimentally at elevated temperature.

Fig. 1a shows that many orderings on BCC and HCP are very close to the convex hull. The hierarchical β_S''' orderings on the HCP crystal structure are found to be energetically competitive between the compositions of 0.125–0.25 [10]. At a composition of 0.25, the $D0_{19}$ ordering on HCP, also known as β" in the Mg literature is energetically degenerate with the β_1 phase. This high degree of degeneracy between the BCC and HCP orderings is likely to persist at higher temperatures.

The formation energies of orderings on the C14-Laves phase are shown in Fig. 1b. The ordering at 1/3 is the well-known Mg_2Y Laves phase. Stoichiometries that deviate from this ideal composition rise rapidly in energy relative to the global convex hull, with excess magnesium being accommodated more easily than yttrium. The formation energies suggest that excess magnesium is accommodated on the yttrium sublattice. Experimental phase diagrams show similar trends with the 4*f* asymmetric site in the Laves phase accommodating the excess magnesium [23].

The calculated formation energies for orderings on α-Mn are shown in Fig. 1c. The ideal stoichiometry of this phase is $Mg_{24}Y_5$, which is predicted to have a formation energy that is within a few meV/atom of the global convex hull. The formation energies in the off-stoichiometric orderings show that this crystal structure is able to tolerate excess magnesium defects but not excess yttrium. The low energy orderings on the metastable convex hull for this phase allow for excess magnesium on the 8*c* Wyckoff position. This is in quantitative agreement with prior experimental results [30].

Free energies of the various phases calculated within the quasi-harmonic approximation show that vibrational excitations play a crucial role in determining relative stability at elevated temperature. We calculated the vibrational free energies of the ground state orderings on BCC, HCP as well as the experimental structures for $Mg_{24}Y_5$ and Mg_2Y. The calculated phase diagram is shown in Fig. 2. At low temperatures, only the β_S', β_1 and B2 phases are predicted to be stable. With increasing temperature, vibrational entropy becomes significant, resulting in the stabilization of the more complex $Mg_{24}Y_5$ and Mg_2Y crystal structures. The appearance of a Laves phase at high temperature also occurs in other Mg-RE

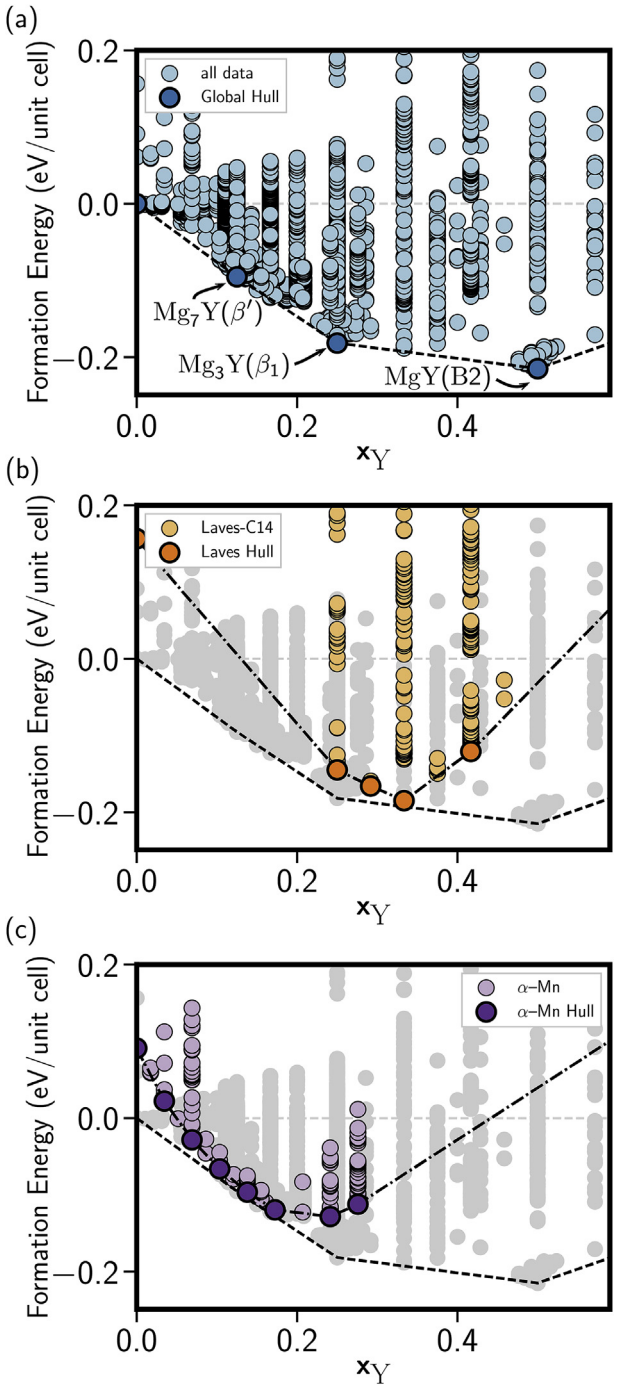

Fig. 1. (A) Global convex hull calculated over all calculated configurations. DFT predicts HCP and BCC based orderings to be stable at 0 K; (B) Formation energies of orderings on the C14-Laves crystal structure; (C) Convex hull orderings on the alpha-Mn crystal structure. The structure is predicted to accommodate magnesium excess but does not tolerate larger yttrium stoichiometries.

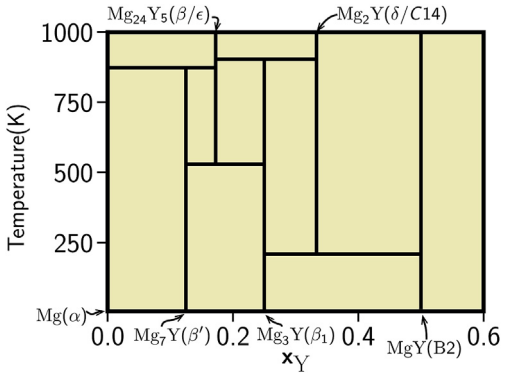

Fig. 2. Phase diagram calculated based on DFT formation energies at 0 K and finite temperature free energies from quasiharmonic phonon calculations.

systems, e.g. Ref. [31]. The Mg_2Y Laves phase becomes stable around 200 K, while β-$Mg_{24}Y_5$ is predicted to become stable above ~520 K. The low-temperature phases disappear completely above 900 K, leading to two-phase regions between the pure elements, β and the Laves phase. The calculated phase diagram does not account for the liquid phase, which in thermodynamic equilibrium appears above 840 K for Mg rich compositions.

The calculated phase diagram predicts that the strengthening β_S'-Mg_7Y phase is thermodynamically stable at low to intermediate temperatures. It indicates that β_S', once formed, will not decompose, but only coarsen, provided aging is performed at low to intermediate temperatures. This is in contrast to other Mg-rare earth binaries such as Mg-Nd [22], where the HCP based β′ and β‴ strengthening phases are metastable and, therefore, susceptible to transformation to more stable phases that are detrimental to mechanical properties. The calculated phase diagram treats all phases as line compounds and therefore neglects contributions to the free energy arising from configurational entropy. Experimental evidence suggests that this is a reasonable approximation since the various phases appear only to tolerate a minor degree of off-stoichiometry.

4.2. Precipitate evolution

The Mg-Y alloy experienced significant age hardening during aging at 473 K, as shown in Fig. 3. Microhardness increased immediately upon aging and remained stable up to 100 h, where it quickly increased again and reached a maximum after about 2500 h. Further aging for up to 13,000 h resulted in a slight decrease in hardness.

The very initial rise in hardness after just a few minutes of aging was previously explained by the formation of small Y-rich clusters [20]. The second increase in hardness between 200 and 400 h coincided the nucleation of a high number density of β_S' precipitates. After 200 h of aging, few β_S' precipitates were observed (Fig. 4a), but by 400 h, a high density of isolated and uniformly distributed precipitates is noted (Fig. 4 b). Concomitantly, precipitate size also increased. Table 1 summarizes average precipitate sizes and number density as a function of aging time. The majority of β_S' precipitates exhibited a rod-like morphology with square cross sections and elongation along the [0001] direction. Fig. 5a illustrates the rod-like shape viewed along the $11\bar{2}0_{Mg}$ zone axis. At 1000 h, precipitates were either connected to one another in pairs along their $\{10\bar{1}0\}_{Mg}$ facets and separated by a stacking fault or connected to each other by strands emanating from their corners (Fig. 4c). The evolution from isolated precipitates to precipitates in pairs was concomitant with a morphological change from square to

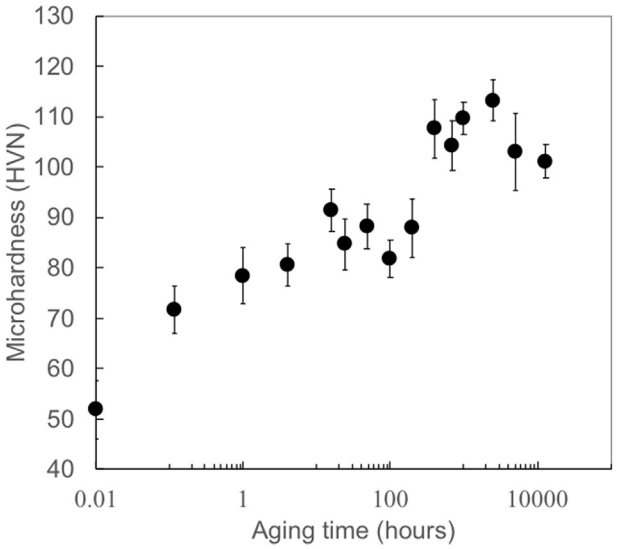

Fig. 3. Microhardness evolution with aging at 473 K.

bell- and hourglass-shaped [0001] cross sections (Fig. 5b). By 2500 h, all precipitates were connected creating a network or cellular arrangement, with preferential alignment along the $11\bar{2}0_{Mg}$ directions (Fig. 4d–f). Within this network, many precipitates had elongated shapes with noticeably longer dimensions along $11\bar{1}0_{Mg}$ directions than along $11\bar{2}0_{Mg}$ directions. From 1000 to 5000 h, the number density of β_S' precipitates and the precipitate dimension along the $\{1\bar{1}00\}$ direction remained constant. The volume fraction of precipitates estimated from the 2D STEM images increased from ~9% at 400 h to ~16% at 1000 h, and remained constant thereafter. The average diameter of the cells, estimated using a line intercept method, increased with aging time, from 124 ± 5 nm at 2500 h, 147 ± 9 nm at 5000 h, to 274 ± 65 nm at 13,000 h. We note that the interface between precipitate and Mg matrix remained coherent, even for the largest precipitates.

Most of the β_S' precipitates were initially decorated with Y-rich strands attached mainly at the corners for isolated precipitates (Fig. 5b). Within cellular arrangements for aging times between 1000 and 2500 h, strands connected precipitates from their corners or along $\{1\bar{1}00\}$ planar edges of the precipitates (Fig. 5c and d). The strands consisted of individual zigzag chains of Y-rich columns lying parallel to $\{10\bar{1}0\}_{Mg}$ planes, identical to the individual $\{010\}_{\beta'}$ planes of the β_S' phase such that the Y-rich columns sit on Mg lattice sites in a triangular pattern. Different strand arrangements were observed, including single strands, and two or more parallel strands separated by a distance that is twice as long as the unit spacing along the b-axis for the β_S' structure (Fig. 5c). With longer aging times, β_S' precipitates within the cellular arrangement connected such that precipitates of the same variant either merged or remained separated by a stacking fault and precipitates of opposite variants remained separated by 3 atomic layers (Fig. 5 d,e).

4.3. Strain energy analysis

The aging experiments showed that the β_S' precipitates initially developed β_S' strands at their corners before becoming interconnected and adopt very specific shapes and orientation relationships (Fig. 4). We hypothesize that such precipitate evolution is driven by a minimization of the overall strain energy and the spatial relationships between precipitates involves interactions between regions of highest strain energy density. To analyze this

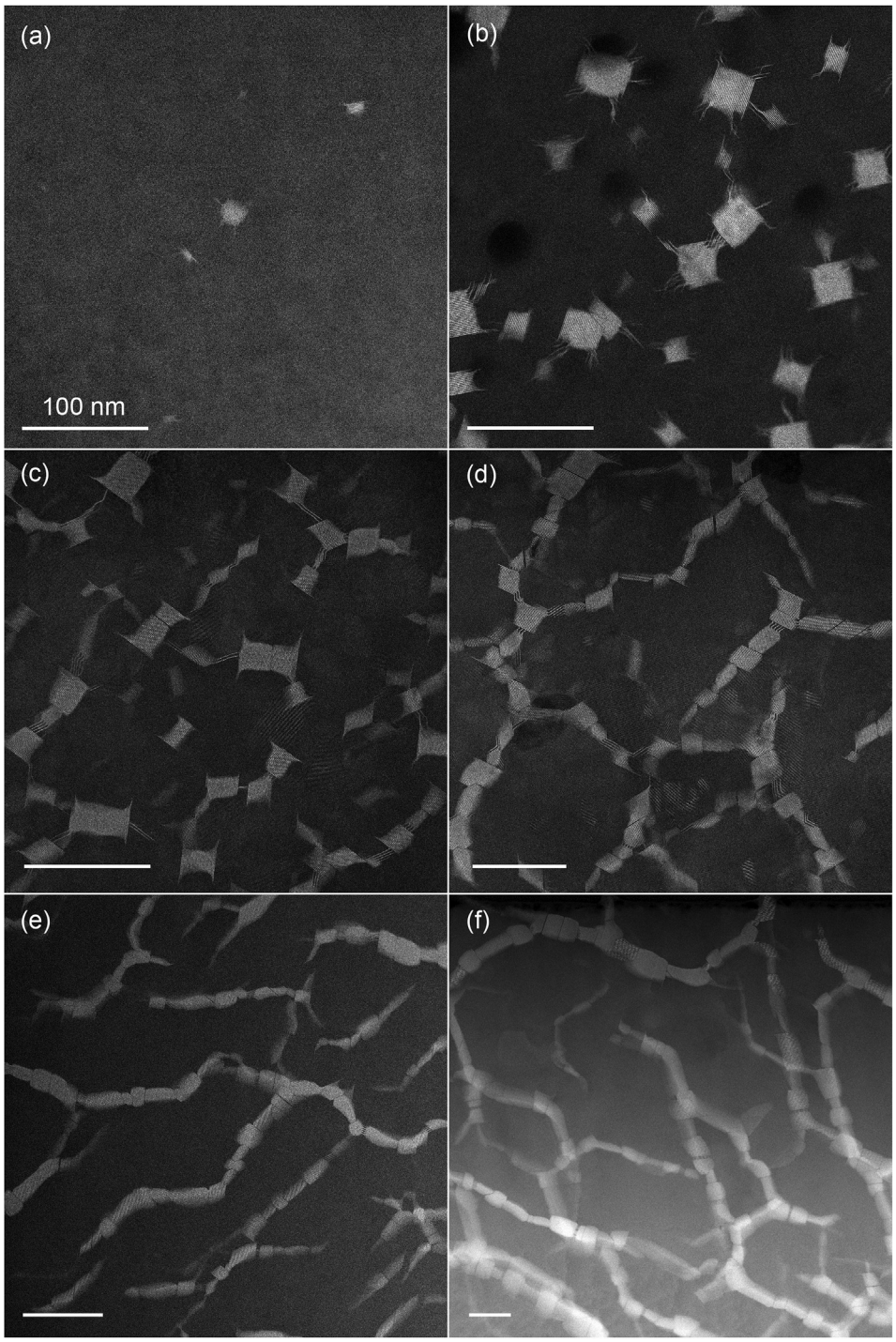

Fig. 4. High angle annular dark field (HAADF) scanning transmission electron microscopy (STEM) images taken along the [0001] zone axis after the aging times of (a) 200 h; (b) 400 h; (c) 1000 h (d) 2500 h; (e) 5000 h; (f) 13,000 h.

Table 1
Average precipitate size along two principal axes and number density of β' precipitates during aging.

Aging time (hours)	200	400	1000	2500	5000
Number density[a] (/10^{20}) (/m3)	6.9 ± 3.3	33 ± 12	45 ± 12	56 ± 26	48 ± 14
L <10-10> (nm)	14 ± 5	19 ± 9	23 ± 9	19 ± 7	20 ± 6
L[0001] (nm)	60	91 ± 38	109 ± 47	–	–

[a] The error on the size measurements is the standard deviation, estimated to be larger than experimental error.

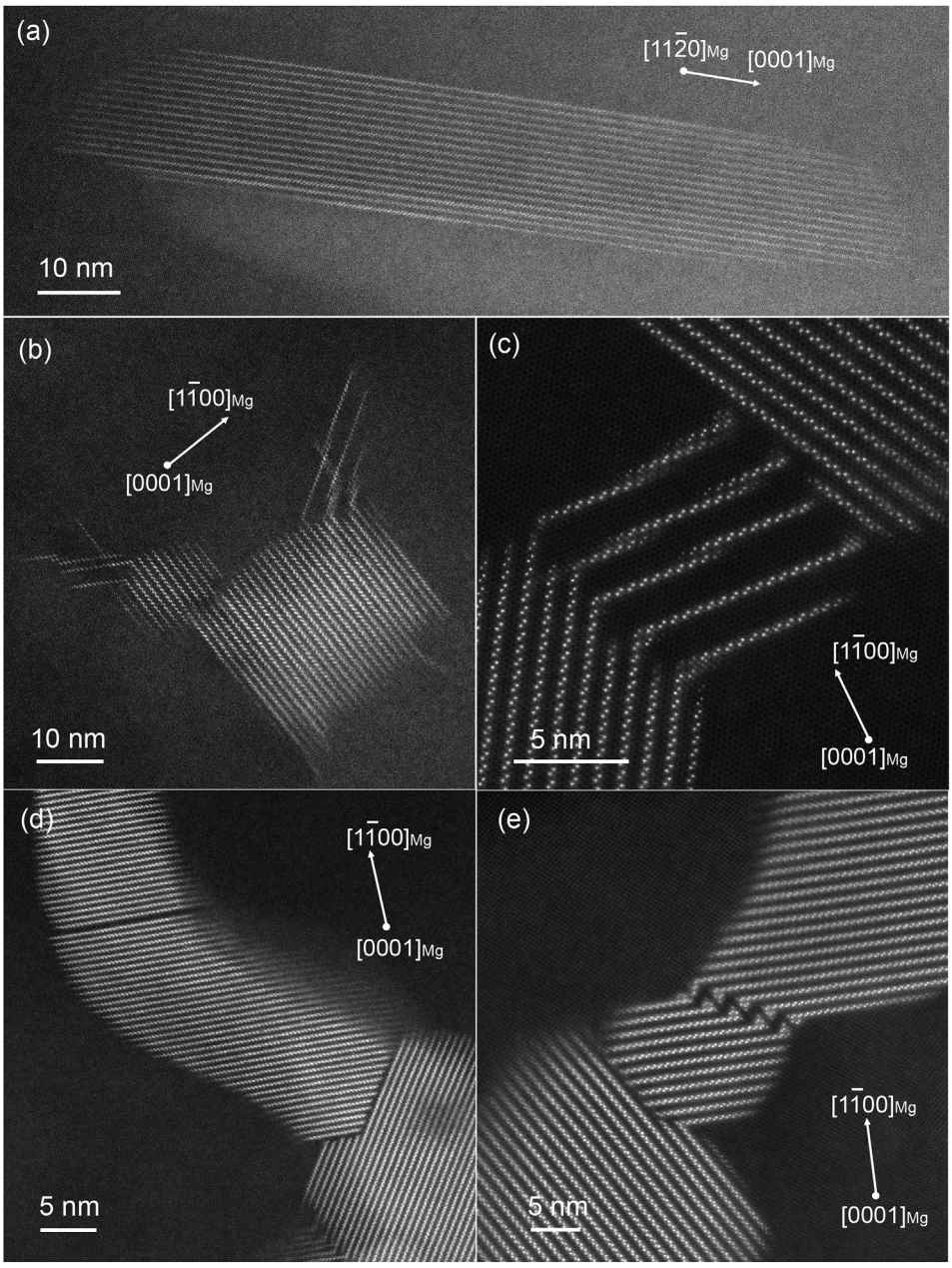

Fig. 5. High angle annular dark field (HAADF) scanning transmission electron microscopy (STEM) images. (a) elongated morphology of isolated β′ precipitates along the [0001] direction – the image was obtained after 400 h of aging; (b) isolated precipitate with Y-rich strands after 400 h, (c) Regularly spaced Y-rich stands connecting 2 precipitate variants within a cell arrangement after 5000 h, (d) two forms of stacking fault separating same precipitate variants (indicated by an arrow) after at 5000 h, and (e) after 13,000 h. (d) and (e) also illustrate close proximity of different variants within the cell arrangements.

hypothesis, we performed finite element calculations of the strain energy of five representative precipitate morphologies. These are shown in Fig. 6. The strain energy density distribution for the simplified configurations was calculated, and thresholded so as to filter out low energy regions and highlight the regions of highest strain energy densities. The corners and faces of the precipitates have the highest strain energy densities as expected due to those being regions of stress concentrations. Nucleation and growth of the β_S' strands would be favored at such location if such event is associated with an overall reduction in strain energy. In addition, some corners appear to have higher energy densities compared to others depending on the variants involved and their arrangement in the microstructure. Again, this may explain the development of preferential arrangements, as seen experimentally, as such arrangement might decreases the strain energy from strain field interactions. Similarly to strands, minimization of the overall strain energy in the system could proceed through nucleation of new precipitates at or near these corner locations. To illustrate the decrease in energy associated with precipitate proximity, the energy density of two isolated precipitates of the same variant is compared to that of a single precipitate that would occur by merging of the two initial precipitates (Fig. 7). For isolated precipitates of length L_p, the distance between the precipitates (d_p) is decreased while the total length ($2L_p + d_p$) is maintained to be constant. The case of $d_p = 0$ models a connected precipitate. The energy decreases with decreasing d_p to L_p ratio, confirming

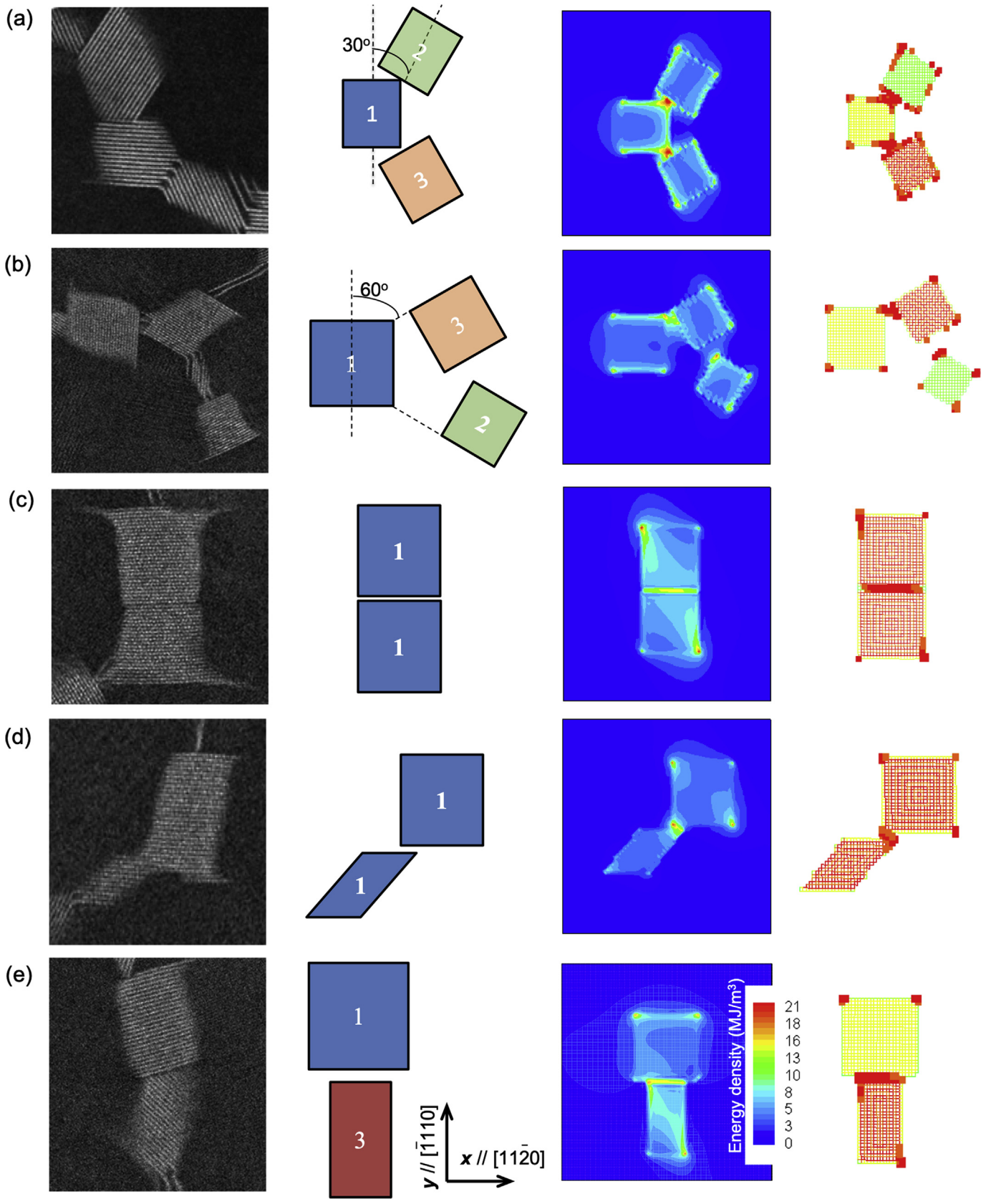

Fig. 6. (left) Different precipitate arrangements simulated with corresponding (right) energy density. The simulations show preferential localization of energies at corners and interfaces. Numbering refers to the different precipitate variants.

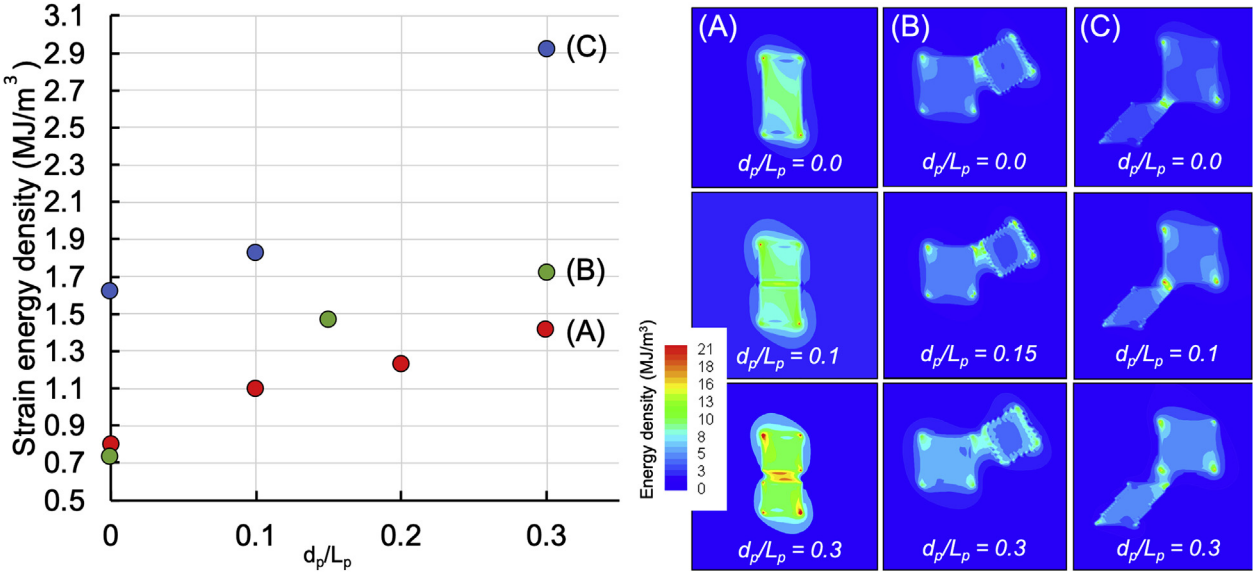

Fig. 7. The strain energy density **E** of the precipitate arrangements in selected configurations shown in Fig. 6 with three different $\mathbf{d_p/L_p}$ ratios reveal that merging of two precipitates yields the least amount of strain energy density.

minimization of the overall energy density when precipitates merge. In effect, the decrease in energy density is partly from the loss of high stress corners when precipitates merge.

5. Discussion

The Mg-Y alloy studied here exhibits a remarkable stability of the β_S' phase with no observation of the β phase after over 13,000 h of aging at 473 K. These observations are in agreement with the calculated phase diagram (Fig. 2), that predicts a two-phase equilibrium between α-Mg and β_S' for the experimentally selected alloy composition and aging temperature. The calculations also suggest that the β phase would become stable at temperatures higher than ~500 K, which is consistent with its absence in the present experiments, and presence in prior work on a Mg-3.0 at.%Y alloy after aging at 623 K [21]. However, while the predicted phase diagram (Fig. 2) is in good qualitative agreement with experimental findings, we note that the predicted transition temperatures are unlikely to be quantitatively precise. There are indeed some quantitative differences. Previous experiments reported the formation of HCP solid solutions, β, and the Laves phase at temperatures around 800 K [32]. Our predicted transition temperatures differ by approximately 100 K. Several contributions to the free energy that have been neglected in the current study, including configurational entropy and anharmonic vibrations that could influence these transition temperatures.

The evolution of the β_S' precipitates during aging highlights the unique contribution of misfit strains. The misfit strain values and dimensions, morphology, and spatial arrangements of the precipitates are consistent with a negligible contribution from interfacial energy. The stress-free transformation strains for β_S' in a Mg matrix are ~2% in the prismatic directions and near 0 along the basal direction [10]. These strains values suggest that precipitates should remain coherent to sizes of the order of 50 nm, and indeed the absence of interfacial dislocations and perfect interfacial coherency are observed experimentally. In the limit of an isotropic cross section, a quick estimation of the critical size defining the transition between small sized particles dominated by surface energy and larger particles dominated by elastic strain energy may be obtained from $6\gamma/\mu\varepsilon^2$, where γ is the interfacial energy (4–30 mJ [11]), μ is the shear modulus of Mg (13.3–19.4 GPa [11]), and ε is the stress-free misfit (~0–0.03 [10]). Focusing on the precipitate cross-section in the basal plane, the estimated critical size is much smaller than the size of the precipitates considered here, suggesting the β_S' precipitates are in a size regime dominated by strain energy.

Strains not only control the internal structure of the precipitates as previously discussed [10,33], but also the precipitate morphological changes during aging, microstructural patterning, and consequently the delayed onset of coarsening. The β_S' morphologies at early times, i.e. square cross section rods, and orientation relationship with the Mg matrix are inconsistent with minimization of interfacial energy alone. Previously calculated DFT interfacial energy values would yield thin plates along $\{11\bar{2}0\}$ planes [34], while the present observations show β_S' precipitates in the shape of elongated rod along the [0001] direction. These shapes were previously well reproduced by phase field simulations of isolated precipitates taking into account elastic strains [34,35].

The changing precipitate morphology during aging is another indication of the role of long range elastic strains. The initially square cross sections for isolated precipitates evolved to concave shapes replaced by elongated shapes when precipitates became interconnected. The square cross-section is reminiscent of the shapes observed in other systems with coherent ordered precipitates such as the Ni/Ni_3Al system, where it was shown that the cubic shape is one of the possible morphologies consistent with strain energy minimization of isolated particles [36]. The bell- and hourglass-shaped precipitate pairs at 1000 h of aging may be another consequence of strain field minimization. Previous simulations found that concave interfaces can be equilibrium characteristics and strongly depend on the exact elastic and misfit symmetry [36]. Alternatively, such concave shapes have also been interpreted as the result of enhanced solute diffusion at the corners [37]. In the present system, irrespective of the cause, the concave interfaces are transient and disappear once a fully connected precipitate cellular structure is formed. At much longer aging times (beyond 5000 h), the elongation of the β_S' precipitate cross section within the cellular structure highlights how strain field interactions can lead to non-equilibrium precipitate morphologies, as was previously observed in a number of other systems with high

volume fractions of coherent precipitates [38].

The volume fraction and number density of β_S' precipitates increases between 200 and 1000 h. At the latter time, the volume fraction was estimated at $16 \pm 2\%$, that is very close to the theoretical equilibrium volume fraction (~17%). At this stage, classical evolution driven by minimization of interfacial energy, or coarsening, would lead to a reduction in number density of precipitates and increase in the average precipitates size. It is evident however that the β_S' precipitates follow a different evolution path. Both number density and size remain constant through aging up to 5000 h. Here, we hypothesize that the alloy evolution is first driven by the reduction of the significant elastic strains that developed from the formation of isolated precipitates. This is consistent with the very low interfacial energy values providing lower driving force for coarsening. As the elastic strain calculations suggest, strain energy minimization leads to spatial alignment of the precipitates, momentarily preventing microstructural coarsening, until the system has reached lower elastic strain energy levels. We also note that the translational and rotational variants of the ordered β_S' phase prevent coalescence of neighboring precipitates that remain separated by stacking faults (Figs. 4 and 5). In other systems such as Ni based alloys [39], strain energy has been reported to slow down and even stall the coarsening process, and lead to the alignment of precipitates by movement of their center of mass, similarly to the present observations. Once the cellular precipitate arrangement formed and aging is increased to longer times, the measurements of the cell size confirms that the overall microstructure coarsens driven by minimization of the surface area.

Finally, the cellular arrangement of β_S' precipitates is associated with peak hardness and significant hardening (Fig. 3), and the decrease in hardness after 5000 h is consistent with coarsening of the cellular structure. While isolated β' precipitates are sheared by basal and prismatic dislocations [40], future work should clarify whether the unique spatial arrangement of precipitates into cells leads to additional strengthening compared to a uniform distribution of spherical precipitates.

6. Conclusions

Phase equilibria and aging behavior of a binary Mg-Y alloy was investigated using a combination of microhardness measurements, scanning transmission electron microscopy, and first principles calculations. The following conclusions were reached:

- For dilute alloys aged at low temperatures, β_S'-Mg_7Y is predicted to be a thermodynamically stable precipitate phase. Experimentally, no other Y-rich phase was observed for the aging times considered here (<13,000 h). This result is in contrast to other Mg-rare earth binaries, where the HCP based β′ and/or β‴ phases are metastable and therefore susceptible to decomposition upon over aging.
- The evolution of the coherent β_S' precipitates follows an unusual path where precipitates nucleate uniformly, then undergo a spatial re-arrangement into an interconnected cellular network.
- The shape evolution of isolated precipitates is consistent with strain field minimization. Precipitates form into elongated rods with initial square cross section that evolve into hourglass and elongated cross sections as precipitates become interconnected. The nucleation of β_S' strands at the corners of β_S' precipitates may also be favored by local strain fields.
- Strain energy retards the onset of coarsening and drives the spatial re-arrangement of β_S' precipitates into a cellular structure. Once the cellular structure is formed, its coarsening driven by interfacial energy minimization, i.e. increase in precipitate size and increase in cell dimensions, takes place.

Acknowledgements

This work was supported by the U.S. Department of Energy - Basic Energy science program [grant award number DE-SC0008637], the University of Michigan Rackham Graduate School (fellowship for E.S.), the Michigan Center for Materials Characterization at the University of Michigan for training and technical support, and Magnesium Elektron Inc. who provided the alloys used in this investigation. The authors also thank Dr. Peng-Wei Chu, David Allen, and Malhar Kute for supervising and performing the last hardness measurement and Dr. Allen Hunter for preparation and imaging one of the TEM samples.

References

[1] I. Polmear, Magnesium alloys and applications, Mater. Sci. Technol. 10 (1994).
[2] J.F. Nie, Precipitation and hardening in magnesium alloys, Metall. Mater. Trans. A 43 (2012) 3891–3939.
[3] T.M. Pollock, Weight loss with magnesium alloys, Science 328 (2010) 986–987.
[4] M. Nishijima, K. Yubuta, K, Hiraga, Characterization of β′ precipitate phase in Mg-2 at%Y alloy aged to peak hardness condition by high-angle Annular detector dark-field scanning transmission electron microscopy (HAADF-STEM), Mater. Trans. 48 (2007) 84–87.
[5] K. Saito, K, Hiraga, The structures of precipitates in an Mg-0.5 at%Nd age-hardened alloy studied by HAADF-STEM technique, Mater. Trans. 52 (2011) 1860–1867.
[6] W. Lefebvre, V. Kopp, C. Pareige, Nano-precipitates made of atomic pillars revealed by single atom detection in a Mg-Nd alloy, Appl. Phys. Lett. 100 (2012).
[7] M. Nishijima, K. Hiraga, M. Yamasaki, Y, Kawamura, Characterization of β′ phase precipitates in an Mg-5 at%Gd alloy aged in a peak hardness condition, studied by high-angle Annular detector dark-field scanning transmission electron microscopy, Mater. Trans. 47 (2006) 2109.
[8] M. Nishijima, K. Hiraga, Structural changes of precipitates in an Mg-5 at% Gd alloy studied by transmission electron microscopy, Mater. Trans. 48 (2007) 10–15.
[9] M. Nishijima, K. Hiraga, M. Yamasaki, Y. Kawamura, Characterization of precipitates in Mg-Sm alloy aged at 200C, studied by high-resolution transmission electron microscopy and high-angle Annular detector dark-field scanning transmission electron microscopy, Mater. Trans. 50 (2009) 1747–1752.
[10] A.R. Natarajan, A. Van der Ven, A unified description of ordering in HCP Mg-RE alloys, Acta Mater. 124 (2017) 620–632.
[11] Y.Z. Ji, A. Issa, T.W. Heo, J.E. Saal, C. Wolverton, L.Q. Chen, Predicting β′ precipitate morphology and evolution in Mg–RE alloys using a combination of first-principles calculations and phase-field modeling, Acta Mater. 76 (2014) 259–271.
[12] S. DeWitt, E.L.S. Solomon, A.R. Natarajan, V. Araullo-Peters, S. Rudraraju, L. Aagesen, B. Puchala, E.A. Marquis, A. Van der Ven, K. Thornton, J.E. Allison, Misfit-driven B'' precipitate composition and morphology in Mg-Nd alloys, Acta Mater. 136 (2017) 378–389.
[13] E.L.S. Solomon, V.J. Araullo-Peters, J.E. Allison, E.A. Marquis, Early precipitate morphologies in Mg-Nd-(Zr) alloy, Scripta Mater. 128 (2017) 14–17.
[14] R. Wilson, C.J. Bettles, B.C. Muddle, J.F. Nie, Precipitation hardening in Mg-3 wt %Nd(-Zn) casting alloys, Mater. Sci. Forum 419–422 (2003) 267–272.
[15] E.L.S. Solomon, T. Chan, A. Chen, B. Uttal-Veroff, E.A. Marquis, Aging Behavior of Mg Alloys Containing Nd and Y, Magnesium Technology, TMS, San Diego, CA, 2017.
[16] X. Gao, J.F. Nie, Enhanced precipitation-hardening in Mg–Gd alloys containing Ag and Zn, Scripta Mater. 58 (2008) 619–622.
[17] T. Pike, B. Noble, The formation and structure of precipitates in a dilute magnesium-neodymium alloy, J. Less Common Met. 30 (1973) 63–74.
[18] E.L.S. Solomon, E.A. Marquis, The Structure of B'' and B' in an Aged Mg-nd Alloy, Magnesium Technology, TMS, Nashville, TN, 2016.
[19] H. Liu, W.F. Xu, N.C. Wilson, L.M. Peng, J.F. Nie, formation of and interaction between BprimeF and Bprime phases in a Mg-Gd alloy, J. Alloy. Comp. 712 (2017) 334–344.
[20] J.F. Nie, N.C. Wilson, Y.M. Zhu, Z. Xu, Solute clusters and GP zones in binary Mg-RE alloys, Acta Mater. 106 (2016) 260.
[21] M.X. Zhang, P.M. Kelly, Morphology and crystallography of Mg24Y5 precipitate in Mg-Y alloy, Scripta Mater. 48 (2003) 379.
[22] Z. Xu, Monash University, 2013.
[23] H. Okamoto, Mg-Y (magnesium-yttrium), J. Phase Equilibria Diffus. 31 (2010), 199–199.
[24] J.C. Thomas, A. Van der Ven, Finite-temperature properties of strongly anharmonic and mechanically unstable crystal phases from first principles, Phys. Rev. B 88 (2013), 214111.
[25] B. Puchala, A. Van der Ven, Thermodynamics of the Zr-O system from first-principles calculations, Phys. Rev. B 88 (2013), 094108.

[26] A. Van der Ven, J.C. Thomas, B. Puchala, A.R. Natarajan, First-principles statistical mechanics of mult-component crystals, Annu. Rev. Mater. Res. 48 (2018) 27–55.
[27] D.M. Barnett, e. al., the strain energy of a coherent ellipsoidal precipitate, Scripta Metall. 8 (1974) 1447–1450.
[28] E. Pan, e. al., Eshelby problem of polygonal inclusions in anisotropic piezoelectric full-and half-planes, J. Mech. Phys. Solid. 52 (2004) 567–589.
[29] M.E. Fitzpatrick, M.T. Hutchings, P.J. Withers, Separation of macroscopic, elastic mismatch and thermal expansion misfit stresses in metal matrix composite quenched plates from neutron diffraction measurements, Acta Mater. 45 (1997) 4867–4876.
[30] F. Bonhomme, K. Yvon, Synthesis and crystal structure refinement of cubic Mg6.8Y, J. Alloy. Comp. 232 (1996) 271–273.
[31] H. Okamoto, Mg-Nd (magnesium-neodymium), J. Phase Equil. 12.2 (249–250) (1991).
[32] H.D. Zhao, G.W. Qin, Y.P. Ren, W.L. Pei, D. Chen, Y. Guo, The maximum solubility of Y in α-Mg and composition ranges of Mg$_{24}$Y$_{5-x}$ and Mg$_{2}$Y$_{1-x}$ intermetallic phases in Mg-Y binadry system, J. Alloys Compd 509 (2011) 627–631.
[33] A.R. Natarajan, E.L.S. Solomon, B. Puchala, E.A. Marquis, A. Van der Ven, On the early stages of precipitation in dilute Mg-Nd alloys, Acta Mater. 108 (2016) 367–379.
[34] H. Liu, Y. Gao, J.Z. Liu, Y.M. Zhu, Y. Wang, J.F. Nie, A simulation study of the shape of beta ' precipitates in Mg-Y and Mg-Gd alloys, Acta Mater. 61 (2013) 453–466.
[35] A. Issa, J. Saal, C. Wolverton, Physical factors controlling the observed high-strength precipitate morphology in Mg-rare earth alloys. Acta Mater.. 65, 240–250 (2104).
[36] M.E. Thompson, C.S. Su, P.W. Voorhees, The equilibrium shape of a misfitting precipitate, Acta Metall. Mater 42 (1994) 2107–2122.
[37] Y. Wang, A.G. Khachaturyan, Shape instability during precipitate growth in coherent solids, Acta Metall. Mater. 43 (1995) 1837–1857.
[38] A.J. Ardell, The effects of elastic interactions on precipitate microstructural evolution in elastically inhomogeneous nickel-base alloys, Phil. Mag. 94 (2014) 2101–2130.
[39] P. Fratzl, O. Penrose, J.L. Lebowitz, Modeling of phase separation in alloys with coherent elastic misfit, J. Stat. Phys. 95 (1999) 1429–1503.
[40] E.L.S. Solomon, E.A. Marquis, Deformation behavior of β′ and β′′′ precipitates in Mg-RE alloys, Mater. Lett. 216 (2018) 67–69.